To be published in Applied Optics:

Title: Optical spanner for nanoparticle rotation with focused optical vortex generated through Pancharatnam-Berry phase metalens

Authors: Zhe Shen,Zhiyuan Xiang,Ziyao Wang,Yaochun Shen,Baifu Zhang

Accepted: 12 May 21

Posted 13 May 21

DOI: https://doi.org/10.1364/AO.425892

Optical spanner for nanoparticle rotation with focused optical vortex generated through Pancharatnam-Berry phase metalens

ZHE SHEN,[1,*] ZHIYUAN XIANG,[1] ZIYAO WANG,[1] YAOCHUN SHEN,[2] AND BAIFU ZHANG[1]

[1]*School of Electronic and Optical Engineering, Nanjing University of Science and Technology, Nanjing 210094, China*
[2]*Department of Electrical Engineering & Electronics, University of Liverpool, Liverpool L69 3GJ, UK*
**shenzhe@njust.edu.cn*

Abstract: Based on the focused optical vortex (OV) generated by metalens, we studied the physical mechanism for optical manipulation of metal (Ag) nanoparticles in the orbital angular momentum (OAM) field. We found that metal nanoparticles can be stably trapped inside the OV ring and rotated by the azimuthal driving force originating from OAM transfer. The azimuthal force and rotation speed are directly and inversely proportional to the particle size, respectively. The torque for the same particle at the OV ring increases with the increase of the topological charge of the metalens. Considering the same topological charge, the radius of the OV ring or the range of the optical spanner has a positive correlation with the focal length. These kinds of optical tweezers by vortex metalens can be used as optical spanner or micro-rotor for lab-on-chip applications.

1. Introduction

In 1986, Ashkin *et al* invented optical tweezers for particle trapping by creating a three-dimensional potential well through a highly focused laser beam with an objective lens [1]. On the basis of optical force, Friese *et al* demonstrated that elliptically polarized laser beam can induce optical torque on the microscopic birefringent particle of calcite [2], a mechanism transferring angular momentum first observed by Beth in 1936 [3]. Furthermore, Allen *et al* found that light beam with Laguerre-Gaussian amplitude distribution has well-defined orbital angular momentum (OAM), which was confirmed by experiments with optical tweezers [4, 5]. After that, the optical tweezers based on Laguerre-Gaussian laser modes were developed for applications of optical spanners [6, 7]. The OAM induced optical force opened up a new research branch for particle manipulation. In recent years, optical vortex (OV) as a light beam with spiral phase and OAM has been widely used to manipulate microscopic objects. Because of its unique properties, it can trap particles and force particles to undergo periodic or non-periodic orbital motion [8-10], which have application prospects in micro-fabrication, catalysis, and biomedical science [11-13]. For example, particle rotation can be used for optical sorting cooperated with a microfluidic chip, thus there is a demand to develop a chip platform for integrated optical spanner.

In the past two decades, with the development of OAM manipulation, generation methods for OV have become diverse, such as using spiral interference patterns [14, 15], holographic phase plate [16], and spatial light modulator (SLM) [17]. In addition, our previous work suggested a new approach to generate plasmonic vortex (PV), which may be a better candidate of optical spanner for metal particles [18]. After that, we specifically studied the force distribution and capture potential of metal particles in PV, proving that PV can stably trap and dynamically rotate metal particles [19]. However, these systems require bulky

devices and microscope objectives, which have the disadvantages of system complexity, unfavorable integration, and low efficiency.

In the last decade, with the superiority of flexibly adjusting and controlling the phase, amplitude, and polarization of transmitted or reflected electromagnetic waves in the desired manner [20-24], metasurfaces have been considered promising two-dimensional metamaterials. According to these characteristics, metasurfaces have been manufactured to be lenses [25-27], waveplates [28-30], polarizers [31-35], and so on. Especially, as an alternative to objective lens, metalens has been used to generate OV and applied to optical tweezers [26, 36]. The nearly two-dimensional, integrable, and flexible phase control characteristics of metalens provide new possibilities for the application of optical spanners.

To our best knowledge, although there are many papers about OV generation through metalens [26, 37-39], the quantitative theoretical analysis of OAM in its focal field has not been carried. In this work, focused OVs with different topological charges were obtained with metalenses, then we studied not only the trapping but also the rotation. The optical forces and trapping potentials of the metal particles in the focal regions were calculated by the finite-difference time-domain (FDTD) method. The effects of particle sizes and topological charges on the velocities and torques were studied in detail. In addition, the influence of focal length on the OAM field and the rotation force were analyzed. This work paves new avenues for the applications of optical spanners and microfluidic motors.

2. Method and Theory

2.1 The Metalens Structure

As shown in Fig. 1(a), through a metalens, normally incident light is focused to form a doughnut-shaped OV, where a metal particle is trapped. All the intensity and phase information were extracted by the frequency-domain monitor in the simulation region. Perfect matching layer (PML) boundaries were used in all directions, the mesh step was 5 nm. Fig. 1(b) shows that the unit cell of the metalens consists of titanium dioxide (TiO_2) nanofins on a silica (SiO_2) substrate. As a half-wave plate, the length, width, and thickness of each nanofin are L = 250 nm, W = 95 nm, and H = 600 nm, respectively. The working wavelength of each nanofin is 532 nm. All the TiO_2 nanofins are arranged in circles from the center to the edge. The spacing between each circle of nanofins is 350 nm. In the same circle, the distance between adjacent nanofins is 325 nm. For high refractive index dielectric metasurfaces, the interaction between the nanofins is negligible, and the light scattered at each nanofin is dominated by the local waveguide effect. Therefore, the transmission coefficient of the unit cell array can be roughly regarded as a single response of the unit cell, and according to reference [26], it can maintain a transmission efficiency up to 90%.

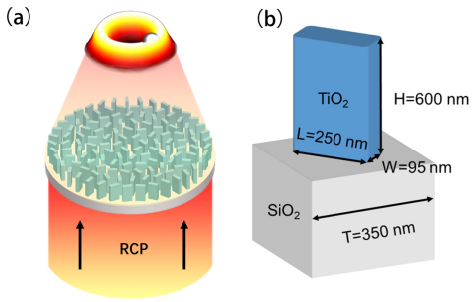

Fig. 1. (a) Schematic diagram of the metalens. (b) The metalens is composed of a titanium dioxide (TiO_2) nanofin and a silica (SiO_2) substrate.

In order to achieve the desired focusing properties of the OV, phase profiles of a spherical convex lens $\varphi_s(x,y)$ and a vortex lens $\varphi_v(x,y)$ are combined for the ultrathin flat lens [26],

$$\varphi(x,y)=\varphi_s(x,y)+\varphi_v(x,y)=\frac{2\pi}{\lambda_{in}}\left(f-\sqrt{x^2+y^2+f^2}\right)+m\arctan\left(\frac{y}{x}\right), \tag{1}$$

where x and y are the horizontal and vertical coordinates, λ_{in} is the wavelength of the incident light, f is the focal length of the lens, and m is the geometrical topological charge of OV. Each nanofin can produce a phase change to the transmitted circularly polarized light by rotating a specific angle. When the right-handed circularly polarized (RCP) light is incident, the rotation of the nanofins will produce a Pancharatnam-Berry (PB) phase [40, 41], and the polarization of the transmitted light will almost become left-handed circularly polarized. This phase change satisfies $\varphi_{nf}(x,y)=2\theta_{nf}(x,y)$, and $\theta_{nf}(x,y)$ is the rotation angle of each nanofin. Therefore, the phase diagram required for the focused OV can be achieved by rotating each nanofin at a given coordinate (x,y) by an angle as follows,

$$\theta(x,y)=\theta_s(x,y)+\theta_v(x,y)=\frac{\pi}{\lambda_d}\left(f-\sqrt{x^2+y^2+f^2}\right)+\frac{m}{2}\arctan\left(\frac{y}{x}\right), \tag{2}$$

2.2 Optical Force, Trapping Potential, Viscosity Resistance, and Torque

The time-averaged optical force applied to a particle can be calculated through the integral of Maxwell stress tensor (MST) on the particle surface [26],

$$<F>=\int\left\{\frac{\varepsilon}{2}\mathrm{Re}[(E\cdot n)E^*]-\frac{\varepsilon}{4}(E\cdot E^*)n+\frac{\mu}{2}\mathrm{Re}[\mu(H\cdot n)H^*]-\frac{\mu}{4}(H\cdot H^*)n\right\}ds\,, \tag{3}$$

where ε and μ are the relative dielectric constant and magnetic permeability of the medium surrounding the particle, respectively, n is the normal unit perpendicular to the integral area ds . The optical force can be obtained by the MST toolbox available in a commercial solver (FDTD solutions, Lumerical). Note that the total force is composed of gradient force and scattering force.

The trapping potential can be calculated by the following formula [42]:

$$U(r_0)=-\int_{\infty}^{r_0}F(r)dr\,, \tag{4}$$

where $U(r_0)$ is the energy required to move a particle from infinity to position r_0 . To obtain a stable trap, a trapping potential depth of more than $10k_BT$ is generally required to overcome the interference from thermal effect [43], where k_B is the Boltzmann constant and T is the temperature.

One-dimensional Langevin equation can be used to describe the linear motion of a trapped particle. Assuming that the motion is at the overdamped limit, the acceleration is negligible in a short distance, and the noise is ignored, the equation can be simplified as [44]

$$\gamma\frac{dq}{dt}=F(q)\,, \tag{5}$$

where q is the generalized displacement coordinate of the particle, $F(q)$ is the optical force exerted the particle at the azimuthal position, and γ is the friction coefficient, which is defined by Stokes' law $\gamma=6\pi\upsilon R$, where R is the radius of the particle and υ is the dynamic viscosity of the medium.

According to Barnett and Allen's nonparaxial theory [45, 46], the torque can be expressed as

$$\Gamma = \frac{P_{\text{abs}}}{\omega}\left[\left(l+\sigma_z\right)+\sigma_z\left(\frac{2kz_{\text{R}}}{2p+l+1}+1\right)^{-1}\right]. \tag{6}$$

where P_{abs} is the absorption power of the particle, ω is the frequency of light, p and l are the mode indices, k is the wavenumber, z_{R} is a length term, σ_z is ± 1 for left- or right-handed circularly polarized light or 0 for linearly polarized light. Γ_n can be expressed as $\Gamma_n = v \cdot R_n$, where n is the topological charge, R_n is the radius of the rotation, and v is the speed.

3. Results and Discussions

3.1 Focused Optical Vortices by Metalenses

To facilitate simulation calculation, metalens was designed to have a radius of 5 μm and a focal length of 2 μm. The rotation angles of all the arranged nanofins were calculated according to Eq. (2). We took m = 3 and m = 5 to design the metalenses, where m is topological charge. Fig. 2 shows that they convert normal incident circularly polarized light into focused OVs. Figs. 2(a) and (d) are the electric field distributions of the focused OVs with topological charges of 3 and 5 in the x-y plane. It can be clearly seen that the increase of the topological charge will lead to larger OV ring. The azimuthal energy flow patterns indicate that OAM has been established inside the OVs. Figs. 2(b) and (e) are the E_x phase distributions of the focused OVs with topological charges of 3 and 5 in the x-y plane. Within the optical field of OV, the phase of E_x changes along the circumferential direction by a fixed period, and the number of this period is consistent with the topological charge. As shown in Figs. 2(c) and (f), the OVs of the two topological charges are focused on the plane at the position of 1.8 μm in the z-direction. This result indicates that the actual focal length of the metalens used to generate focused OV agrees with the designed focal length and remains unchanged when m increases from 3 to 5. This demonstrates the flexibility of the metalens that the focal length and topological charge of the focused OV can be designed for specific need.

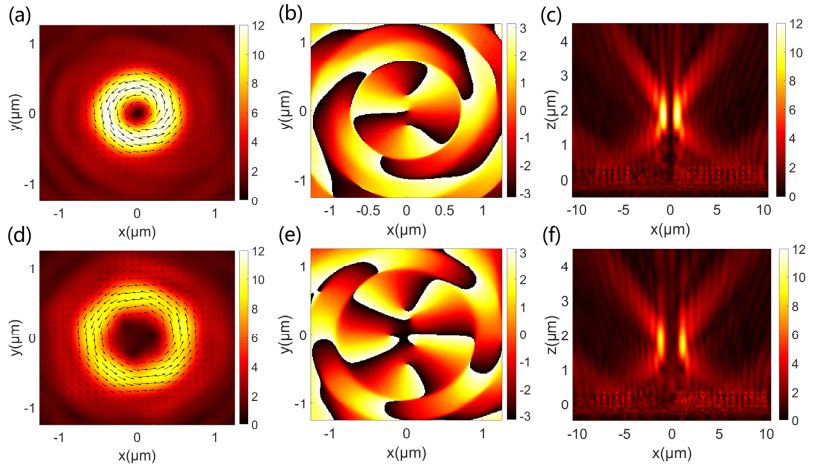

Fig. 2. (a)(d) The electric intensities of focused OVs with topological charges of 3 and 5 in the focal x-y planes. The arrows indicate the time-averaged Poynting vectors of the OVs. (b)(e) The corresponding E_x phase distributions in the focal x-y planes. (c)(f) The corresponding electric

intensities in the propagation x-z planes. The interface between nanofin and substrate is at z = 0 μm.

3.2 Trapping of Metal Nanoparticles in Focused Optical Vortices

In order to obtain the force and behavior of the metal particle in the focal vortex field, we used FDTD and MST methods to numerically calculate the force distribution on the particle. On the basis of the metalenses that have been designed in Sect. 3.1, we put an Ag particle with a radius of 300 nm on the focal plane to calculate the force on the particle. In the simulation, the power of the incident light was 0.79 mW, the medium around Ag nanoparticle was water (n_m = 1.33), which was not embedded around the nanofins for practical consideration. Depending on the radius of the focused OV ring, we decided to take every 0.1 μm as a measurement point from $x = -1.5$ μm to $x = 1.5$ μm in the x-direction ($y = 0$) and then calculated the force of the Ag particle according to Eq. (3).

Figures 3(a), (b) and (c) shows the radial distributions of the forces in the radial, azimuthal, and z- directions, respectively, of the Ag particle in the focal plane of focused OV with topological charge of 3. Note that all the curves appeared in this work were fitted with the least square method. As shown in Fig. 3(a), when the Ag particle moves from the edge to the center, it is first subject to a repulsive force, until it moves into the OV ring, it is subjected to force pointed to the center, which potentially confines the particle. As shown in Fig. 3(b), the azimuthal forces on the Ag particle in the focal vortex field are all along the direction that E_x phase varies. The direction of the azimuthal force is consistent with that of energy flow in Fig. 2(a), and this tangential force provide necessary condition for OAM rotation of particles. As the Ag particle moves from the edge to the center, the absolute value of the azimuthal force first increases and then decreases. Its extremum values are formed at positions close to the OV ring. As shown in Fig. 3(c), F_z always points to the positive direction of the z-axis because of the forwarding scattering, when the particle is within the range of the OV ring, it maintains a relatively high value as the size of OV ring is comparable with that of the particle. Thus, it can overcome the gravity force and achieve the z-direction manipulation.

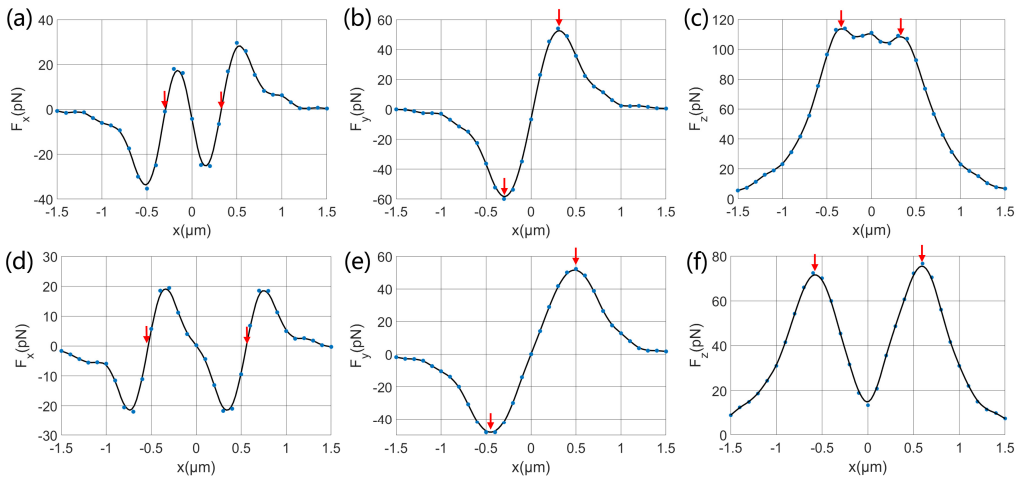

Fig. 3. The distributions along the radial direction of forces in (a) x-, (b) y-, and (c) z- direction of a 300 nm Ag particle in the field of focused OV with topological charge of 3. (d-f) The same force distributions in the field of OV with topological charge of 5. The red arrows indicate the positions of the OV rings.

The lower row of Fig. 3 shows the force distributions of the Ag particle in the field of focused OV with topological charge of 5. Comparing with the result in Fig. 3(a), the morphology of the force distribution of the particle remains the similar. Since the OV ring

becomes larger, both the peak and valley values of F_x move radially outward, which results in a larger range of potential well. Similarly, in Fig. 3(e), the peak value of the azimuthal force provided by the phase change of OV also shifts radially outward. In Fig. 3(f), as the Ag particle moves from the edge to the center, the F_z of the particle increases first and then decreases. Its peak and valley are formed at the position at the ring and the center of OV, respectively, which is different from that in Fig. 3(c). As the ring of OV with topological charge of 5 is larger than the size of the particle, the scattering force is lowest at the central dark spot due to the phase singularity. This result proves that OV can manipulate Ag nanoparticles in the radial and longitudinal directions. The azimuthal force arising from the phase gradient in the circular direction has the potential to be applied to optical spanners.

Furthermore, with these force distributions, we calculated the trapping potential depths in two cases of OV tweezers with topological charges of 3 and 5, by using Eq. (4). As shown in Figs. 4(a) and (b), potential wells are generated and the potential depths inside the OV rings are $1.6\times10^3 k_{\mathrm{B}}T$ and $1.8\times10^3 k_{\mathrm{B}}T$, respectively, which are two orders of magnitude larger than $10k_{\mathrm{B}}T$, indicating that the particle can be stably trapped. Obviously, the field of focused OV with a larger topological charge can produce even larger trapping range and deeper potential well. Notice that the potential wells are asymmetrical and the valleys are off-center. The former is the result of the nonuniformity of the focal fields, which can be attributed to the differences of real-ideal phase and transmittance coefficients. The latter error can be attributed to the mesh size used in the simulation and that the potential wells were calculated with the integral of finite force ranges from left.

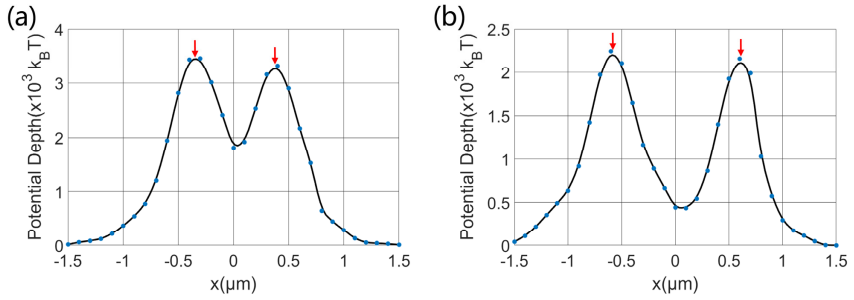

Fig. 4. Potential depths of an Ag particle along the radial direction in the fields of focused OVs with topological charges of (a) 3 and (b) 5. The red arrows indicate the positions of the OV rings.

3.3 Rotation of Metal Nanoparticles in Focused Optical Vortices

Generally, the change of the topological charge will change the size of the OV ring, and the size of the Ag particle will also affect its force distribution in the focal OV field. To investigate the rotational dynamics and confirm the relationship between OAM and topological charge, we numerically studied the effects of Ag particles radius (100 nm ~ 400 nm) and OV topological charge (1 ~ 6) on the optical force and behavior of the particle. We placed the Ag particle at the maximum intensity ring (x = 0.37 μm) of OV with topological charge of 3 and measured the azimuthal force of the particle every 50 nm from 100 nm to 400 nm. Since OV is a circular light field, according to its symmetry, we can measure the force of the metal nanoparticle at one point to represent the characteristics of the circle where this point is located. After that, the instantaneous azimuthal velocity of the particle was calculated according to Eq. (5). From Fig. 5(a), it can be seen that the azimuthal force of the Ag particle increases with the particle diameter, because of the increase of the scattering cross-section. In Fig. 5(a), as the radius of the Ag particle increases, the instantaneous azimuthal velocity of the particle decreases, which is consistent with Eq. (5) that the instantaneous azimuthal velocity

of the particle is directly and inversely proportional to the F_φ and radius of particle, respectively. Although larger scattering cross-section of the Ag particle can be lead to larger F_φ, the instantaneous azimuthal velocity of the particle decreases because of the viscous resistance.

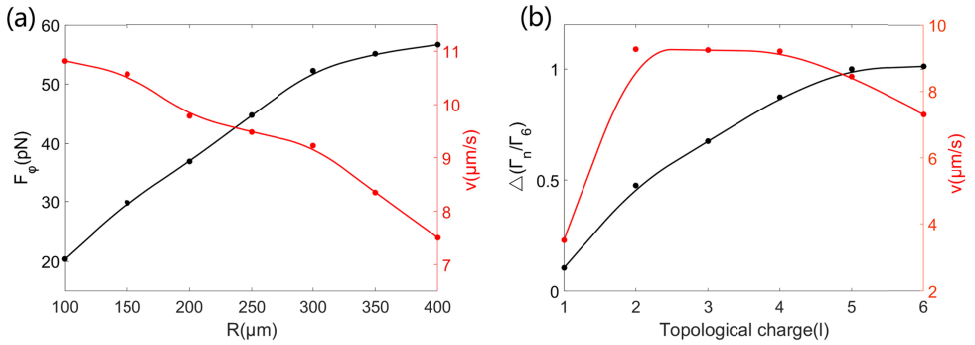

Fig. 5. Influences of particle radius and topological charge on the force. (a) The azimuthal force exerted on Ag particle with different sizes (black curve) and the corresponding rotation speed (red curve) at the maximum intensity ring of OV with topological charge of 3. (b) The distribution of Δ (black curve) and rotation speed (red curve) of the Ag particle at the maximum intensity ring of OV with topological charge from 1 to 6.

Similarly, we calculated the azimuthal force of the Ag particle with a radius of 300 nm at the maximum intensity ring of OV with topological charge from 1 to 6. The instantaneous azimuthal velocity of the Ag particle increases first and then decreases with topological charge. It should be noticed that the increasing of the radius and range of OV ring eventually reduce the average intensity of OV ring. According to $\Gamma_n = v \cdot R_n$ derived from Eq. (6), the torque can be obtained by calculating the instantaneous azimuthal velocity. Therefore, we defined the ratio of torques between $n = 1$ and $n = 6$ as $\Delta = \Gamma_n / \Gamma_6$ to describe the relationship between the particle motion state and topological charge. As expected from Eq. (6), the torque distribution shown in Fig. 5(b) is proportional to the topological charge. With larger topological charge, light in OV carries larger OAM, which can provide larger torque for the rotation of the particle. This also laid the foundation for the application of flexible optical spanners based on the OV generated by metalens.

3.4 Effect of Focal Length for Optical Vortex and Related Force

In order to study the effect of focal length for focused OV, we utilized the method of controlling a single variable by choosing a fixed topological charge and changing focal length. In the case of focused OV with topological charge of 3, we selected focal lengths, from 2 μm to 10 μm at a step size of 1 μm, to design metalenses. Under the same conditions, we conducted simulation calculations to obtain the focal OV fields. Fig. 6(a) shows the relationship between the radii of the OV rings and the focal lengths of the metalenses. Considering the influence of diffraction, the diameter was taken as the distance D between the maximum electric field intensity points on a ring. It can be clearly seen that as the focal length increases, the radius of the OV ring increases linearly. This feature enriches the flexibility of OV tweezers based on metalens. For different sizes of metal particles, the appropriate radius of the OV ring can be obtained by choosing the proper focal length of metalens.

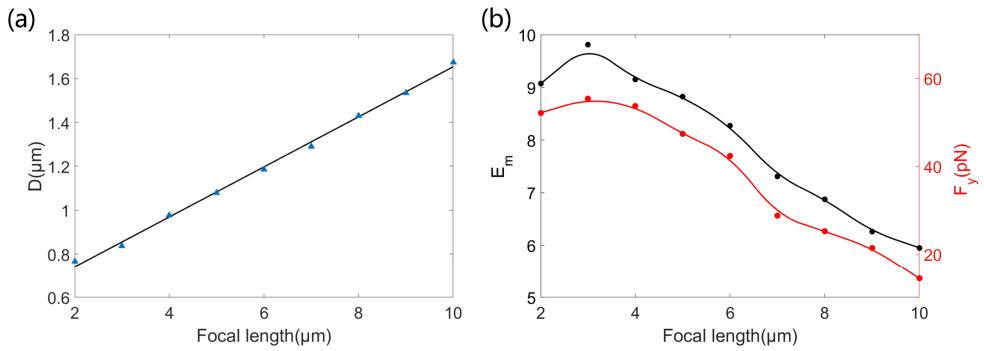

Fig. 6. (a) Relationship between the radii of the OV rings and the focal lengths of the metalenses. The blue dots indicate the radius distribution of the OV ring. The black line is fitted by using the least square method. (b) The distribution of E_m (black curve) of the focal OV field and F_y (red curve) of the Ag particle at the maximum intensity ring of focused OV with focal length from 2 μm to 10 μm.

Subsequently, we calculated the maximum value of the normalized electric field intensity (E_m) in these OV fields. Then, we placed an Ag nanoparticle with radius of 300 nm at the maximum intensity ring of the OV field for the simulation of the azimuthal force the particle subject. As shown in Fig. 6(b), with the increase of focal length, the trends of E_m and F_y are similar. Both of them have peaks at the focal length about 3 μm and then decline. As the increase of the radius of the OV ring will lead to a decrease in the intensity of the focused OV field under the same incident conditions. Consequently, the azimuthal force the particle subject will also decrease. This can be explained according to our previous work [47] that the magnitude of the driving force of metal nanoparticle along the direction of phase gradient is linearly related to the phase gradient.

4. Conclusion

In summary, we numerically studied focused vortex metalenses with different topological charges (3 and 5). It was shown that the metalens can flexibly control the focused OV field by changing the designed topological charge. By calculating force distribution and trapping potential, we found that metal nanoparticles can be stably trapped inside the OV ring. In addition, we verified OAM of the generated OV by metalens through detailed analysis of the particle rotation characteristics. We found that the azimuthal force and rotation velocity were directly proportional and inversely proportional to the particle size, respectively. As the topological charge increases, the torque of metal particles with the same size at the OV ring increases. Furthermore, we demonstrated that the size of the OV ring has a positive correlation with the focal length within the focal length range of our study (2 μm ~ 10 μm), but the maximum intensity value will decrease as the focal length becomes larger. Both the radius of the OV ring and the range of the optical spanner can be controlled by selecting appropriate focal length and topological charge, and this provides a great degree of flexibility for shaping force and manipulating particles. Therefore, the manipulation of particles by vortex metalens is versatile, and it is possible to be applied in optical spanners, micro-rotors, lab-on-a-chip devices, and other related fields.

Funding

National Natural Science Foundation of China (NSFC) (61805119; 61604073); Natural Science Foundation of Jiangsu Province (BK20160839; BK20180468; BK20180469); Fundamental Research Funds for the Central Universities (30919011275).

Disclosures

The authors declare no conflicts of interest.

Data Availability Statement

The data that support the findings of this study are available within the article.

References

1. A. Ashkin, J. M. Dziedzic, J. E. Bjorkholm, and S. Chu, "Observation of a single-beam gradient force optical trap for dielectric particles," Opt. Lett. **11**, 288-290 (1986).
2. M. E. J. Friese, T. A. Nieminen, N. R. Heckenberg, and H. Rubinsztein-Dunlop, "Optical alignment and spinning of laser-trapped microscopic particles," Nature **394**, 348-350 (1998).
3. R. A. Beth, "Mechanical detection and measurement of the angular momentum of light," Phys. Rev. **50**, 115-125 (1936).
4. L. Allen, M. W. Beijersbergen, R. J. C. Spreeuw, and J. P. Woerdman, "Orbital angular momentum of light and the transformation of Laguerre-Gaussian laser modes," Phys. Rev. A **45**, 8185-8189 (1992).
5. A. O'Neil, I. MacVicar, L. Allen, and M. Padgett, "Intrinsic and extrinsic nature of the orbital angular momentum of a light beam," Phys. Rev. Lett. **88**, 053601 (2002).
6. N. B. Simpson, L. Allen, and M. J. Padgett, "Optical tweezers and optical spanners with Laguerre–Gaussian modes," J. Mod. Opt. **43**, 2485-2491 (1996).
7. N. B. Simpson, K. Dholakia, L. Allen, and M. J. Padgett, "Mechanical equivalence of spin and orbital angular momentum of light: an optical spanner," Opt. Lett. **22**, 52-54 (1997).
8. J. Ng, Z. Lin, and C. T. Chan, "Theory of optical trapping by an optical vortex beam," Phy. Rev. Lett. **104**, 103601 (2010).
9. M. Gecevičius, R. Drevinskas, M. Beresna, and P. G. Kazansky, "Optical tweezers with tunable orbital angular momentum," in *CLEO: 2014, OSA Technical Digest (online) (Optical Society of America, 2014)*, paper JTh2A.32.
10. S. Mei, K. Huang, T. Zhang, M. Q. Mehmood, H. Liu, C. T. Lim, J. Teng, and C. -W. Qiu, "Evanescent vortex: Optical subwavelength spanner," Appl. Phys. Lett. **109**, 191107 (2016).
11. D. G. Grier, "A revolution in optical manipulation," Nature **424**, 810-816 (2003).
12. J. E. Curtis, and D. G. Grier, "Structure of optical vortices," Phys. Rev. Lett. **90**, 133901 (2003).
13. G. D. M. Jeffries, J. S. Edgar, Y. Zhao, J. P. Shelby, C. Fong, and D. T. Chiu, "Using polarization-shaped optical vortex traps for single-cell nanosurgery," Nano Lett. **7**, 415-420 (2007).
14. L. Paterson, M. P. MacDonald, J. Arlt, W. Sibbett, P. E. Bryant, and K. Dholakia, "Controlled rotation of optically trapped microscopic particles," Science **292**, 912 (2001).
15. M. P. MacDonald, L. Paterson, K. Volke-Sepulveda, J. Arlt, W. Sibbett, and K. Dholakia, "Creation and manipulation of three-dimensional optically trapped structures," Science **296**, 1101-1103 (2002).
16. M. Harwit, "Photon orbital angular momentum in astrophysics," Astrophys. J. **597**, 1266-1270 (2003).
17. H. Zang, C. Zheng, Z. Ji, X. Liu, Y. Tian, L. Wei, Q. Fan, X. Wang, L. Cao, and E. Liang, "Multiple optical vortices generated by azimuthal fractal spiral zone plates based on liquid crystal spatial light modulator," Optik **175**, 344-350 (2018).
18. Z. Shen, Z. J. Hu, G. H. Yuan, C. J. Min, H. Fang, and X. C. Yuan, "Visualizing orbital angular momentum of plasmonic vortices," Opt. Lett. **37**, 4627-4629 (2012).
19. Y. Zhang, W. Shi, Z. Shen, Z. Man, C. Min, J. Shen, S. Zhu, H. P. Urbach, and X. Yuan, "A plasmonic spanner for metal particle manipulation," Sci. Rep. **5**, 15446 (2015).
20. N. K. Grady, J. E. Heyes, D. R. Chowdhury, Y. Zeng, M. T. Reiten, A. K. Azad, A. J. Taylor, D. A. R. Dalvit, and H.-T. Chen, "Terahertz metamaterials for linear polarization conversion and anomalous refraction," Science **340**, 1304 (2013).
21. A. V. Kildishev, A. Boltasseva, and V. M. Shalaev, "Planar photonics with metasurfaces," Science **339**, 1232009 (2013).
22. X. Ni, N. K. Emani, A. V. Kildishev, A. Boltasseva, and V. M. Shalaev, "Broadband light bending with plasmonic nanoantennas," Science **335**, 427 (2012).
23. N. Yu, P. Genevet, M. A. Kats, F. Aieta, J. -P. Tetienne, F. Capasso, and Z. Gaburro, "Light propagation with phase discontinuities: generalized laws of reflection and refraction," Science **334**, 333 (2011).
24. A. Berrier, B. Gompf, L. Fu, T. Weiss, and H. Schweizer, "Optical anisotropies of single-meander plasmonic metasurfaces analyzed by Mueller matrix spectroscopy," Phys. Rev. B **89**, 195434 (2014).
25. M. Khorasaninejad, W. T. Chen, R. C. Devlin, J. Oh, A. Y. Zhu, and F. Capasso, "Metalenses at visible wavelengths: Diffraction-limited focusing and subwavelength resolution imaging," Science **352**, 1190 (2016).
26. Y. Ma, G. Rui, B. Gu, and Y. Cui, "Trapping and manipulation of nanoparticles using multifocal optical vortex metalens," Sci. Rep. **7**, 14611 (2017).
27. J. B. Pendry, "Negative refraction makes a perfect lens," Phys. Rev. Lett. **85**, 3966-3969 (2000).
28. J. Hu, X. Zhao, Y. Lin, A. Zhu, X. Zhu, P. Guo, B. Cao, and C. Wang, "All-dielectric metasurface circular dichroism waveplate," Sci. Rep. **7**, 41893 (2017).

29. A. Zhu, Q. Qian, Y. Yan, J. Hu, X. Zhao, and C. Wang, "Ultrathin plasmonic quarter waveplate using broken rectangular annular metasurface," Opt. Laser Technol. **92**, 120-125 (2017).
30. X. Zhao, J. Schalch, J. Zhang, H. R. Seren, G. Duan, R. D. Averitt, and X. Zhang, "Electromechanically tunable metasurface transmission waveplate at terahertz frequencies," Optica **5**, 303-310 (2018).
31. J. K. Gansel, M. Thiel, M. S. Rill, M. Decker, K. Bade, V. Saile, G. von Freymann, S. Linden, and M. Wegener, "Gold helix photonic metamaterial as broadband circular polarizer," Science **325**, 1513 (2009).
32. Y. Zhao, M. A. Belkin, and A. Alù, "Twisted optical metamaterials for planarized ultrathin broadband circular polarizers," Nat. Commun. **3**, 870 (2012).
33. J. Liu, Z. Li, W. Liu, H. Cheng, S. Chen, and J. Tian, "High-efficiency mutual dual-band asymmetric transmission of circularly polarized waves with few-layer anisotropic metasurfaces," Adv. Opt. Mater. **4**, 2028-2034 (2016).
34. H. Kurosawa, B. Choi, Y. Sugimoto, and M. Iwanaga, "High-performance metasurface polarizers with extinction ratios exceeding 12000," Opt. Express **25**, 4446-4455 (2017).
35. K. Meng, S. J. Park, L. H. Li, D. R. Bacon, L. Chen, K. Chae, J. Y. Park, A. D. Burnett, E. H. Linfield, A. G. Davies, and J. E. Cunningham, "Tunable broadband terahertz polarizer using graphene-metal hybrid metasurface," Opt. Express **27**, 33768-33778 (2019).
36. G. Tkachenko, D. Stellinga, A. Ruskuc, M. Chen, K. Dholakia, and T. F. Krauss, "Optical trapping with planar silicon metalenses," Opt. Lett. **43**, 3224-3227 (2018).
37. M. Shengtao, M. Q. Mehmood, H. Kun, and Q. Cheng-Wei, "Multi-foci metalens for spin and orbital angular momentum interaction," in *Proc. SPIE, Metamaterials, Metadevices, and Metasystems* **9544**, 95441J (2015).
38. N. Mahmood, I. Kim, M. Q. Mehmood, H. Jeong, A. Akbar, D. Lee, M. Saleem, M. Zubair, M. S. Anwar, F. A. Tahir, and J. Rho, "Polarisation insensitive multifunctional metasurfaces based on all-dielectric nanowaveguides," Nanoscale **10**, 18323-18330 (2018).
39. Z. Li, W. Liu, Z. Li, C. Tang, H. Cheng, J. Li, X. Chen, S. Chen, and J. Tian, "Nonlinear metasurfaces: tripling the capacity of optical vortices by nonlinear metasurface," Laser & Photon. Rev. **12**, 1870049 (2018).
40. M. V. Berry, "The adiabatic phase and pancharatnam's phase for polarized Light," J. Mod. Opt. **34**, 1401-1407 (1987).
41. S. Pancharatnam, "Generalized theory of interference and its applications," P. Indian AS., Sect. A **44**, 398-417 (1956).
42. L. Novotny, R. X. Bian, and X. S. Xie, "Theory of nanometric optical tweezers," Phys. Rev. Lett. **79**, 645-648 (1997).
43. A. H. J. Yang, T. Lerdsuchatawanich, and D. Erickson, "Forces and transport velocities for a particle in a slot waveguide," Nano Lett. **9**, 1182-1188 (2009).
44. Z. Yan, M. Sajjan, and N. F. Scherer, "Fabrication of a material assembly of silver nanoparticles using the phase gradients of optical tweezers," Phys. Rev. Lett. **114**, 143901 (2015).
45. S. M. Barnett, and L. Allen, "Orbital angular momentum and nonparaxial light beams," Opt. Commun. **110**, 670-678 (1994).
46. M. Friese, J. Enger, H. Rubinsztein-Dunlop, and N. Heckenberg, "Optical angular-momentum transfer to trapped absorbing particles," Phys. Rev. A **54**, 1593-1596 (1996).
47. Z. Shen, Z. Wang, H. Liu, and Y. C. Shen, "Optical trapping and separation of metal nanoparticles by cylindrical metalenses with phase gradients," IEEE Photon. J. **99**, 1-10 (2020).